Copyright © 1989, by the author(s).
All rights reserved.

Permission to make digital or hard copies of all or part of this work for personal or classroom use is granted without fee provided that copies are not made or distributed for profit or commercial advantage and that copies bear this notice and the full citation on the first page. To copy otherwise, to republish, to post on servers or to redistribute to lists, requires prior specific permission.

OXIDATION OF SILICON IN AN ECR OXYGEN PLASMA: KINETICS, PHYSICO-CHEMICAL AND ELECTRICAL PROPERTIES

by

D. A. Carl, D. W. Hess, and M. A. Lieberman

Memorandum No. UCB/ERL M89/98

21 August 1989

OXIDATION OF SILICON IN AN ECR OXYGEN PLASMA: KINETICS, PHYSICO-CHEMICAL AND ELECTRICAL PROPERTIES

by

D. A. Carl, D. W. Hess, and M. A. Lieberman

Memorandum No. UCB/ERL M89/98

21 August 1989

ELECTRONICS RESEARCH LABORATORY

College of Engineering
University of California, Berkeley
94720

OXIDATION OF SILICON IN AN ECR OXYGEN PLASMA: KINETICS, PHYSICO-CHEMICAL AND ELECTRICAL PROPERTIES

by

D. A. Carl, D. W. Hess, and M. A. Lieberman

Memorandum No. UCB/ERL M89/98

21 August 1989

ELECTRONICS RESEARCH LABORATORY

College of Engineering
University of California, Berkeley
94720

Oxidation of Silicon in an ECR Oxygen Plasma: Kinetics, Physico-Chemical and Electrical Properties

D. A. Carl, D. W. Hess (Dept. of Chemical Engineering)
and
M. A. Lieberman (Dept. of Electrical Engineering and Computer Science).
University of California, Berkeley, CA

ABSTRACT

An electron cyclotron resonance (ECR) plasma system was used to oxidize single crystal silicon. Two distinct oxidation processes were observed: an ion flux controlled process and a process occurring outside of the ion flux. Oxidation of trench structures confirmed the existence of these two oxidation regimes. Kinetic rate studies indicated that the effective activation energies for both oxidation processes were substantially lower than the activation energy of atmospheric pressure steam or dry oxidation. The Deal-Grove linear-parabolic rate law can be used to describe long time ion controlled oxidation rates although the theory of Wolters-Zegers-van Duynhoven best described the observed oxidation rates. Oxides grown in the ion flux controlled regime had growth rates and physico-chemical properties nearly identical to thermal oxides grown at atmospheric pressure and above 1223 K, whereas oxides grown outside of this regime were self limiting (≈ 100 Å) in thickness and of poorer dielectric quality unless subjected to a post oxidation anneal. Electrical properties of the oxides were investigated with MOS capacitor structures. Capacitance-voltage (C-V) and current-voltage (I-V) studies indicated that the fixed charge density was approximately 1×10^{11} cm^{-2} and that the breakdown strengths were at or above 10 MV cm^{-1}.

I. INTRODUCTION

As thermal budgets for VLSI processing become more stringent and as device dimensions continue to decrease, the need for low temperature thin film processing techniques becomes increasingly critical. These demands have made ECR plasmas the subject of recent intense research and development efforts.[1-9] ECR plasmas have much higher fractional ionization (up to 10%), longer ion and energetic neutral mean free paths and lower maximum ion energies than conventional rf parallel plate discharges.[2] Although significant efforts have been mounted in the application of ECR discharges to thin film etching and deposition, substantially less information has been reported on ECR assisted oxidation. Oxidation of single crystal

silicon in an ECR discharge at 623 K with rates comparable to atmospheric pressure thermal oxidations at 1123 K has previously been reported.[8] Plasma oxidation of silicon has been a subject of interest for many years.[10-15] The kinetics and mechanisms involved are complicated by the plasma environment and thus are not yet fully understood. In this study we examined the effects of plasma parameters and substrate conditions on film growth rate and on physico-chemical/electrical properties of the oxide films. The abilities of the Deal-Grove linear-parabolic and the Wolters-Zegers-van Duynhoven ion space-charge limited growth models to describe oxidation rates were also considered.

II. EXPERIMENTAL APPARATUS AND PROCEDURES

The ECR system used in these experiments is shown in Fig. 1. A 2.45 GHz, 800 W CW microwave power supply/matching network was connected by a WR284 rectangular waveguide through a quartz window to the cylindrical vacuum chamber. Two electromagnets driven in a mirror configuration established an axial B field. Two and three inch diameter <100> and <111> p-type 10-50 ohm-cm single crystal silicon wafers were clamped onto an aluminum holder via a retention ring. The aluminum holder contained resistive heating elements and a thermocouple for substrate temperature control. Aluminum was chosen for the substrate holder because: 1) it has excellent heat transfer characteristics, and 2) aluminum and silicon form an eutectic at 800 K; it could therefore be determined when this temperature was reached or exceeded due to plasma heating of the substrate. Optical emission (Plasma Therm PSS-2) was used to monitor plasma emission and to aid in tuning optimization. A Langmuir probe was used to determine plasma densities (n_i) and electron temperatures (T_e) as functions of radial and axial position. Finally, a small wire loop was utilized as an rf field detector to determine if any microwave power passed through the ECR zone reached the substrate.

To grow a film, a wafer was placed into the system, and the system was evacuated to $\approx 1 \times 10^{-4}$ Pa and heated to the desired substrate temperature. Oxygen was then input through a calibrated rotameter and an MKS 248A Pressure Control Valve connected to an MKS 250B Pressure Control System. When the desired pressure and flow rate were attained, microwave power was applied. Oxide film thicknesses were

measured via ellipsometry (Gaertner Model L116A). Fourier transform infrared spectroscopy (FTIR), x-ray photoelectron spectroscopy (XPS) and oxide etch rates in (5:1) $HF:H_2O$ oxide etchant were used to characterize the physical and chemical properties of the oxides. MOS capacitor structures were fabricated from representative samples. C-V and I-V electrical testing was performed with an HP 4200A 1 MHz Capacitance Meter/C-V Plotter connected to an HP 9836U computer prior to and after a 673 K 30 minute sinter in forming gas. The bias temperature stress gate potentials were + 1 V or - 1 V at a temperature of 473 K for 5 minutes.

III. RESULTS AND DISCUSSION

A. Discharge Characteristics

Langmuir probes were used to determine n_i and T_e over a wide range of input power, gas pressure and magnetic field strengths via the method of Laframboise.[16] One of the most interesting features of this particular ECR configuration involves the observation that there may be several high and low stable modes of operation for a given set of external parameter settings. In fact, plasma density changed more than an order of magnitude from low to high mode with only slight perturbations (1 to 5%) in tuning or input power. In the so-called "low mode," significant reductions in ion density and in input microwave power absorption occurred. Possible causes for such high density mode to low density mode shifts are currently being investigated. Most oxidations performed were in the high mode of operation in which essentially all the incident microwave power was absorbed at the ECR zone, no microwave power reaches the substrate and maximum ion was density obtained. As shown in Fig. 2, the ion density increased linearly with power in the high mode regime. Below $P_{forward} \approx 150$ W, only low mode could be sustained. The effect of magnetic field strength on ion density for a $P_{forward} = 700$ W and O_2 pressure of 1.3×10^{-1} Pa is shown in Fig. 3. A maximum density was achieved at an input magnet current of 150 A, corresponding to an ECR zone at the mirror midplane. The ion density was essentially independent of pressure over the range of 6.5×10^{-2} to 5.8×10^{-1} Pa. T_e also was relatively insensitive to pressure, power and position; values typically ranged from 4 to 5 eV. Ion densities increased monotonically from the wafer holder to the ECR region

along the axis of the chamber, reaching a value as high as 3×10^{12} cm^{-3} at $P_{forward}$ = 700 W.

The optical emission system was used to monitor atomic, ionic and impurity emissions as functions of the discharge parameter space; Fig. 4 shows a typical emission spectrum. Emission intensities for most observed peaks increased with power in the high mode regime and were relatively insensitive to flow rate from 5 to 30 sccm. The intensity of the 525 nm O_2^+ emission tracked the ion density measured by Langmuir probing. Thus the system was used as a non-intrusive means of determining optimum tuning, i.e. maximizing ion density, for a particular $P_{forward}$, pressure and flow rate.

B. Oxidation Results

If ion flux is controlling the oxidation rate, then anything done to shadow, mask, divert or significantly decrease the ion beam from the surface of the wafer should change the apparent oxidation rate and alter the physico-chemical and/or electrical properties of the oxide. Since the sample holder assembly was rotatable, the wafer could be placed at any angle to the incident ECR plasma flux. As the holder was turned, the retention ring cast a "shadow" on portions of the wafer to be oxidized. Under this shadow the oxide formed was much thinner and less dense than the oxide formed in the ion flux. In another experiment, a 5 x 5 x 1.5 mm quartz window was placed 2 cm in front of the wafer in the ECR plasma stream during oxidation. This window passed most energetic photons (down to 200 nm)[17] while blocking ion flux and energetic neutral flux from the ECR source region. A sharp pattern transfer was observed on the oxidized wafer, indicating that ion flux or energetic neutral flux was primarily responsible for the high oxidation rate process. A small permanent magnet was placed 1 cm behind the wafer holder during several oxidations; a small spot of increased oxide thickness was observed on the wafer immediately in front of the magnet. Finally, the rate of ion controlled oxidation tracked with ion flux. Maximum oxidation rates were obtained when I_{magnet} was 150 A and $P_{forward}$ = 700 W. These conditions correspond to the maximum ion density observed (Fig. 2 and Fig. 3). In summary, blocking or modifying the ion flux changed the oxide growth rates, indicating that this flux is critical to high growth rate oxide formation.

The strongest indication that ion flux was responsible for the higher rate oxidation process comes

from transmission electron microscopy (TEM) analysis of oxidized trench structures. Table I shows sidewall oxide thickness vs. top oxide thickness for polysilicon trench structures, 0.6 μm high by 1 μm wide on thermal SiO_2. The sidewall thicknesses were quite uniform from top to bottom. Clearly, the primary difference between the sidewall and top of such a structure was ion flux; photons and hot neutrals should be omnidirectional and their respective fluxes should not change much over such a small distance. Thus the second, slower oxidation process occurring on sidewalls apparently was not ion controlled, but more probably was atomic oxygen controlled. This sidewall oxidation, outside of the ion flux, matched oxidation rates observed when the plasma was operating in the low density mode ($P_{forward}$ < 150 W) and when the ion flux was diverted or masked from the surface in high density mode. For the low mode, the ion density, and hence the ion flux, is typically a factor of 20 smaller than for high density mode; e.g. $n_i \approx 5 \times 10^9$ cm^{-3} in low mode at $P_{forward}$ = 150 W while $n_i \approx 1 \times 10^{11}$ for the same forward power in the completely absorbing high mode. Indeed, the low mode oxidation process (and therefore the sidewall and out of flux oxidation processes as well) matched the results of Kimura et al and Vinckier et al with respect to activation energy (0.3 to 0.4 eV) even though Vinckier's conditions were substantially different.[15]

i. **Deal-Grove Analysis of Ion Flux Controlled Oxidation**

The Deal-Grove[18] oxidation model has been in use for many years and the details of the derivation and the parameter definitions may be found elsewhere. The primary result of the model is that thermal oxidation follows the relation:

$$\frac{x}{A/2} = \left[1 + \frac{t+\tau}{A^2/4B}\right]^{1/2} - 1 \qquad [1]$$

where x is the oxide thickness, t is the oxidation time and τ, A and B are empirical constants based upon a derived pseudo steady-state linear transport and first order reaction model. In Eqn. [1], B is the parabolic rate constant while the ratio of B/A is the linear rate constant.

Fig. 5 shows a plot of oxide thickness vs. time for various effective powers. Fig. 6 shows the effect of temperature on oxide thickness vs. time for a $P_{forward}$ = 400 W and 1.3×10^{-1} Pa oxidation condition and the associated plot of oxide thickness vs. the ratio of oxidation time to oxide thickness. The

slope of the lines in the latter plot is the parabolic rate constant, B, while the intercept is the negative of the A parameter in Eqn. [1]. Table II summarizes the rate constants obtained via this analysis. Activation energies in high mode for the linear rate coefficient as well as the parabolic rate coefficient are on the order of 0.06 to 0.1 eV. As ion density increased with increasing power, the apparent activation energy decreased, reaching zero at $P_{forward}$ = 700 W. Obviously, oxidation rates were controlled by different processes in high mode compared to low mode operation. Furthermore, each operating mode differed substantially from atmospheric thermal oxidation.

Deal and Grove observed that the 2.1 eV activation energy obtained from their analysis of thermal oxidation was nearly the same as the Si-Si bond energy; it was assumed that Si-Si bond breaking was the rate limiting step. The low activation energies observed in the present study indicate an alternate rate limiting step. Negative values of the linear rate coefficient, B/A have been reported for some plasma oxidation processes.[8] These results have been explained by assuming that O^- transport through the growing oxide is the rate limiting step. However, our analyses did not yield negative values for B/A. The DG model assumes that the parabolic rate process should have an activation energy the same as that of O_2 diffusing through quartz--clearly not the case in ion flux controlled ECR oxidation. Thus, although the data may be fit with the DG model, the values for the physical constants obtained indicate that ECR oxidation proceeds by different mechanisms. Since the wafer is placed directly in the plasma during ECR oxidation, a large field may be generated across the oxide due to self bias. This field may facilitate rapid transport of ionic species through the growing oxide. Such a field assisted process could account for a lower activation energy of the parabolic rate constant, but does not explain the low activation energy for the linear rate constant. Vacuum ultraviolet (VUV) photon flux may also affect the temperature dependence of both the linear and the parabolic rate constants through Si-Si bond breaking and oxide defect formation.

ii. Wolters - Zegers-van Duynhoven Analysis

Recent work by Wolters and Zegers-van Duynhoven (WZ) has shown that the kinetics of dry oxidation can be described by a power law oxidation model.[19] This approach modifies the classical oxidation theory of Wagner by considering the effect of internal electric fields on ion conduction. The WZ model

has an advantage over the Deal-Grove model in that it can correlate published data for dry thermal oxidation throughout the entire oxide thickness range from native oxide thickness to final oxide thickness. According to WZ, oxidation can be described by:

$$\frac{dx_{ox}}{dt} = Cx_{ox}^{-\beta} \qquad [2]$$

which has the solution

$$x_{ox} = C^{*}t^{\alpha} \qquad [3]$$

where C is an effective rate coefficient (i.e. driving force times the ionic conductivity), β is a measure of field barrier height induced by positive or negative space charge, $\alpha = (\beta + 1)^{-1}$ and $C^{*} = (C/\alpha)^{\alpha}$.[20] A plot of the logarithm of oxidation time versus the logarithm of oxide thickness yields a straight line with slope α and intercept $\log(C^{*})$. From the value for α, β can be calculated. Fig. 7 shows the WZ log-log plots obtained from analysis of the ion flux controlled ECR oxidation results and Table III lists the empirical constants obtained. Wolters and Zegers-van Duynhoven calculated an activation energy of 2.22 eV for the rate constant C for thermal dry oxidation, which agrees well with the DG effective activation energy of 2.1 eV.

Fig. 7 indicates that the WZ model describes well our ECR oxidation results. The driving force was enhanced substantially in the ECR plasma to allow oxidation processes to occur at rates equivalent to atmospheric oxidation 400 K higher temperature. This increased effective rate can be viewed as an increase in the either the driving force of ion conductivity, an increase in ion conductivity or both. The ion flux controlled ECR oxidation occurs at a rate similar to dry oxidation at 1173 K as observed by Wolters and Zegers-van Duynhoven, but again, the effective activation energy for the ECR oxidation process is nearly zero (0.11 eV). The plasma may induce substantial fields in the growing oxide and VUV photon flux could generate conditions in the oxide which account for the enhanced rate. Thus the WZ physical assumptions of space-charge transport may describe the physical processes involved in ECR oxidation and therefore account for the excellent data fit.

C. Orientation Dependance

The oxidation rate of <111> Si was approximately 1.1 times greater than <100> Si under the same high mode ECR plasma conditions at $P_{forward}$ = 700 W and 1.3 x 10^{-1} Pa. This was established both by oxidizing wafers independently and by breaking wafers of different crystal orientation into two pieces and oxidizing the two halves of different crystal orientation simultaneously. The latter process was repeated with the orientation of the wafers rotated 90° to verify that angular position on the wafer holder did not influence the results. The standard deviation of thickness variation on the wafers oxidized in this experiment were on the order of 2%; the factor of 1.1 is greater than the error associated with the measurement.

D. Physical Film Characterization

FTIR, XPS and etch rate in oxide etchant were used as means of comparing the physical and chemical properties of ECR oxides to thermal oxides grown at 1223 K in dry oxygen. The 1070 cm^{-1} IR Si-O absorbance peak has been used as an indication of film stress as well as film density,[21] where an absorbance shift to a higher wavenumber has been interpreted as an increase in film density and bond strength. If the ECR oxide was grown at the same rate as the thermal oxide, the Si-O absorbance at 1070 cm^{-1} are virtually identical. Etch rates in (5:1) HF:H_2O were ≈ 50 nm/min for ECR oxides, essentially the same as for thermal oxides. Within the resolution of these methods of analysis (≈1-5%), no detectible physical or chemical difference existed between these films.

E. Electrical Characterization

MOS structures were fabricated on the ECR oxides by evaporation of 1.7 x 10^{-2} cm diameter aluminum dots through shadow masks. Fig. 8 shows the room temperature high frequency C-V curve for a 22 nm ECR oxide grown at $P_{forward}$ 700 W, 623 K and 1.3 x 10^{-1} Pa and temperature stressed (398 K) high frequency response. Mobile ion contamination was not observed during bias temperature stress studies. Although the curve closely matches ideal behavior, a slight negative flatband shift most likely attributable to VUV photon damage in the ECR processing environment is evident. Dielectric constants were 3.5 to

4 and breakdown strengths were ≈ 10 MV cm^{-1}. Therefore, although the silicon oxides were grown in a plasma environment, the electrical characteristics were not drastically altered by plasma radiation damage. The MOS capacitor structures were tested prior to and after aluminum sintering. Before sintering, MOS structures showed flatband shifts on the order of 5 or more volts for 50 nm films. Bias temperature stress reduced the flatband voltage shifts. It is unclear if this low temperature (>473 K) treatment modified the aluminum-silicon interface or annealed radiation damage. Sintered MOS structures exhibited electrical characteristics close to thermal oxides.

CONCLUSIONS

An ECR oxygen plasma has been used to grow silicon oxides with physical, chemical and electrical properties similar to those of high temperature (>1000 K) thermally grown oxides.. Two distinct oxidation processes were observed; a rapid ion flux controlled oxidation process and a slower, self-limiting oxidation occurring out of the ion flux. The ion flux controlled oxidation has an effective activation energy that is nearly zero, whereas the out of ion flux oxidation process had an activation energy of approximately 0.3 to 0.4 eV. Reasonable fits were obtained from application of the Deal-Grove linear-parabolic oxidation model but the physical constants obtained indicated that the oxidation was controlled by different mechanisms than the Deal-Grove model. The space charge limited growth--power law oxidation model of Wolters and Zegers-van Duynhoven more closely fit the data. The exact mechanisms involved in both the low mode and high mode oxidations are still unclear and will be further investigated. Investigation of MOS capacitor structures using these oxides suggests that these films may be suitable for gate dielectrics in VLSI and ULSI devices.

ACKNOWLEDGEMENTS

This work was supported by National Science Foundation Grant Nos. ECS-8517363 and ENG-8710988, Department of Energy Grant No. DE-FG03-87ER13727, and a contract from IBM General Technology Div., Burlington, VT. The authors would like to thank S. V. Nguyen of IBM for the TEM analysis, A. H. Sato and J. Steinhauer for their assistance in the n_i, T_e, and B field measurements and J. N. Chiang for the XPS surface analysis.

REFERENCES

1. T. Ono, C. Takahashi and S. Matsuo, *Jpn. J. Appl. Phys.* **23**, L534 (1984).

2. T. Ono, M. Oda, C. Takakashi and S. Matsuo, *J. Vac. Sci. Tech.* **B 4**, 696 (1986).

3. K. Suzuki, K. Ninomiya, S. Nishimatsuo and S. Okudaira, *J. Vac. Sci. Tech.* **B 3**, 1025 (1985).

4. T. Unagami and T. Takeshita, *IEEE Trans. on Elec. Dev.* **36**, No. 3, 529 (1989).

5. C. Keqiang, Z. Erli, W. Jinfa, Z. Hansheng, G. Zuoyao and Z. Bagwei, *J. Vac. Sci. Tech.* **A 4**, 828 (1986).

6. I. Nagai, T. Takahagi, A. Ishitani and H. Kuroda, *J. Appl. Phys.* **64**, 5183 (1988).

7. T. V. Herak, T. T. Chau, D. J. Thomson and S. R. Mejia, *J. Appl. Phys.* **65**, 2457 (1989).

8. S. Kimura, E. Murakami, K. Miyake, T. Warabisaka, H. Sunami and T. Tokuyama, *J. Electrochem. Soc.* 1460 (1985).

9. K. Skidmore, *Semiconductor International*, June, 74 (1989).

10. J. Kraitchman, *J. Appl. Phys.* **38**, 4223 (1967).

11. S. Gourrier and M. Bacal, *Plasma Chem. and Plasma Proc.* **1**, No. 3, 217 (1981).

12. A. K. Ray and A. Reisman, *J. Electrochem. Soc.*, 2460 (1981).

13. A. K. Ray and A. Reisman, *J. Electrochem. Soc.*, 2466 (1981).

14. C. Vinckier, P. Coeckelberghs, G. Stevens and S. De Jaegerer, *Appl. Surf. Sci.* **30**, 40 (1987).

15. C. Vinckier, P. Coeckelberghs, G. Stevens and S. De Jaegerer, *J. Appl. Phys.* **62**, 1450 (1987).

16. J. G. Laframboise, Inst. for Aero. Stud., Univ. of Toronto, Rep. No. 100 (1966).

17. W. G. Driscoll and W. Vaugham, ed., *Handbook of Optics*, McGraw-Hill, 7-24 (1978).

18. B. E. Deal and A. S. Grove, *J. Appl. Phys.* **36**, 3770 (1965).

19. D. R. Wolters and A. T. A. Zegers-van Duynhoven, *J. Appl. Phys.* **65**, 5126 (1989).

20. D. R. Wolters and A. T. A. Zegers-van Duynhoven, *J. Appl. Phys.* **65**, 5134 (1989).

21. W. A. Pliskin, *J. Vac. Sci. Tech.* **14**, 1064 (1977).

FIGURES

Fig. 1: Schematic of ECR processing chamber and axial **B** field profile for r=0. The ECR resonance occurs when the magnitude of **B** is 875 Gauss.

Fig. 2: Plot of ion density vs. $P_{forward}$ for ECR O_2 discharge at 1.3 x 10^{-1} Pa and I_{magnet} = 150 A. The ion density is linear with power in this high mode regime.

Fig. 3: Plot of ion density vs. current to the magnet coils for a 1.3 x 10^{-1} Pa discharge at $P_{forward}$ = 700 W.

Fig. 4: Typical optical emission spectra for 1.3 x 10^{-1} Pa, $P_{forward}$ = 500 W ECR O_2 discharge.

Fig. 5: Plot of oxide thickness vs. time for various high mode ECR plasma powers.

Fig. 6: Plot of the effect of temperature on oxide thickness for $P_{forward}$ = 400 W High Mode ECR Plasma and the associated Deal-Grove analysis plot. The slope of the Deal-Grove plot is equal to the parabolic rate constant, B, and the intercept is -A. τ was found to be ≈ 0 for this analysis.

Fig. 7: Plots of Log(oxide thickness) vs. Log(oxidation time) and Log(oxidation rate) vs. Log(oxide thickness) for $P_{forward}$ 400 W high mode ECR oxidation. The slope of the first curve is α with intercept of Log(C^*) from the WZ space-charge oxidation model. The slope of the second curve is β.

Fig. 8: High frequency C - V plots of ECR oxide under normal conditions and temperature stressed at 398 K.

Table I: **Top vs. Sidewall Thickness for Trench Structures Oxidized at .13 Pa, 180 A I_{magnet} as measured via TEM**

$P_{forward}$	Temperature	Sidewall Thickness, Å	Top Thickness, Å	Time, min
700 W	623 K	50	83	2.5
700 W	623 K	50	170	5
700 W	723 K	60	152	5

Table II: **Deal-Grove Model Constants for ECR Oxidation at .13 Pa and Thermal Oxidation Comparison**

$P_{forward}$	Temperature	B (μ^2/h)	A (μ/h)	B/A (μ/h)
700 W	-	0.0126	0.060	0.2096
400 W	623 K	0.00209	0.0179	0.117
400 W	723 K	0.00454	0.0259	0.175
Thermal Ox.	1273K	0.00117	0.165	0.071
Thermal Ox.	1373 K	0.027	0.090	0.30

Table III: **Wolters and Zegers-van Duynhoven Constants for ECR Oxidation at .13 Pa and Thermal Oxidation**

$P_{forward}$	Temperature	α	β	C^* (Å/h)	C (Å/h)
700 W	-	0.714	0.399	2714	8920
400 W	623 K	0.664	0.515	1444	4795
400 W	723 K	0.659	0.505	2266	9779
Thermal Ox.	1073 K	0.670	0.490	60	297
Thermal Ox.	1223 K	0.630	0.590	312	5673
Thermal Ox.	1273 K	0.620	0.600	544	15195

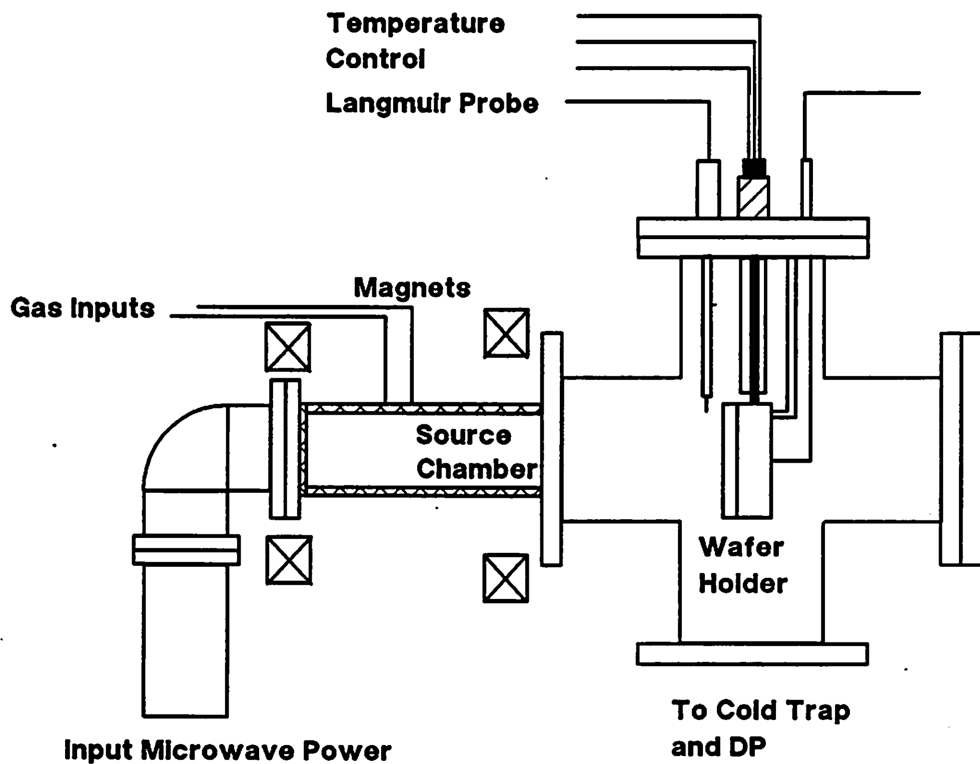

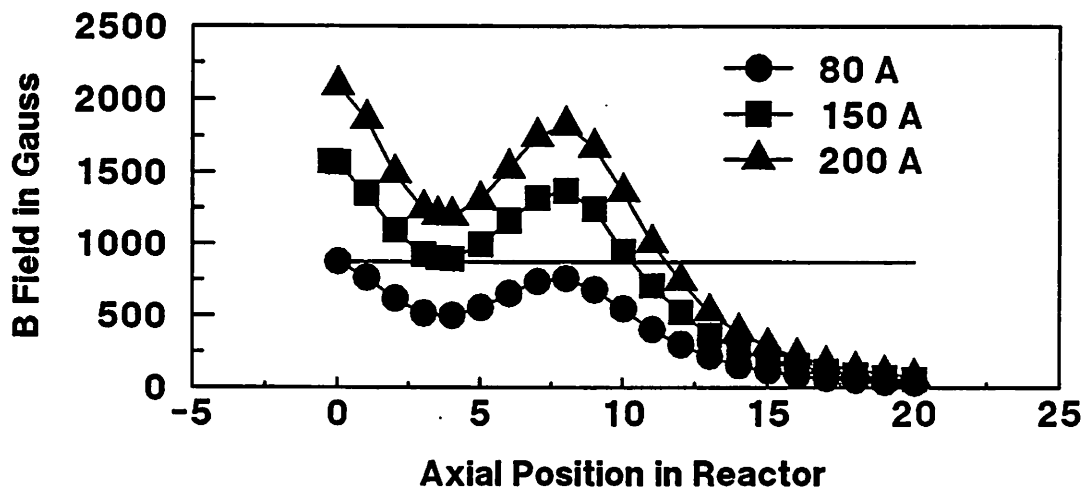

Fig. 1

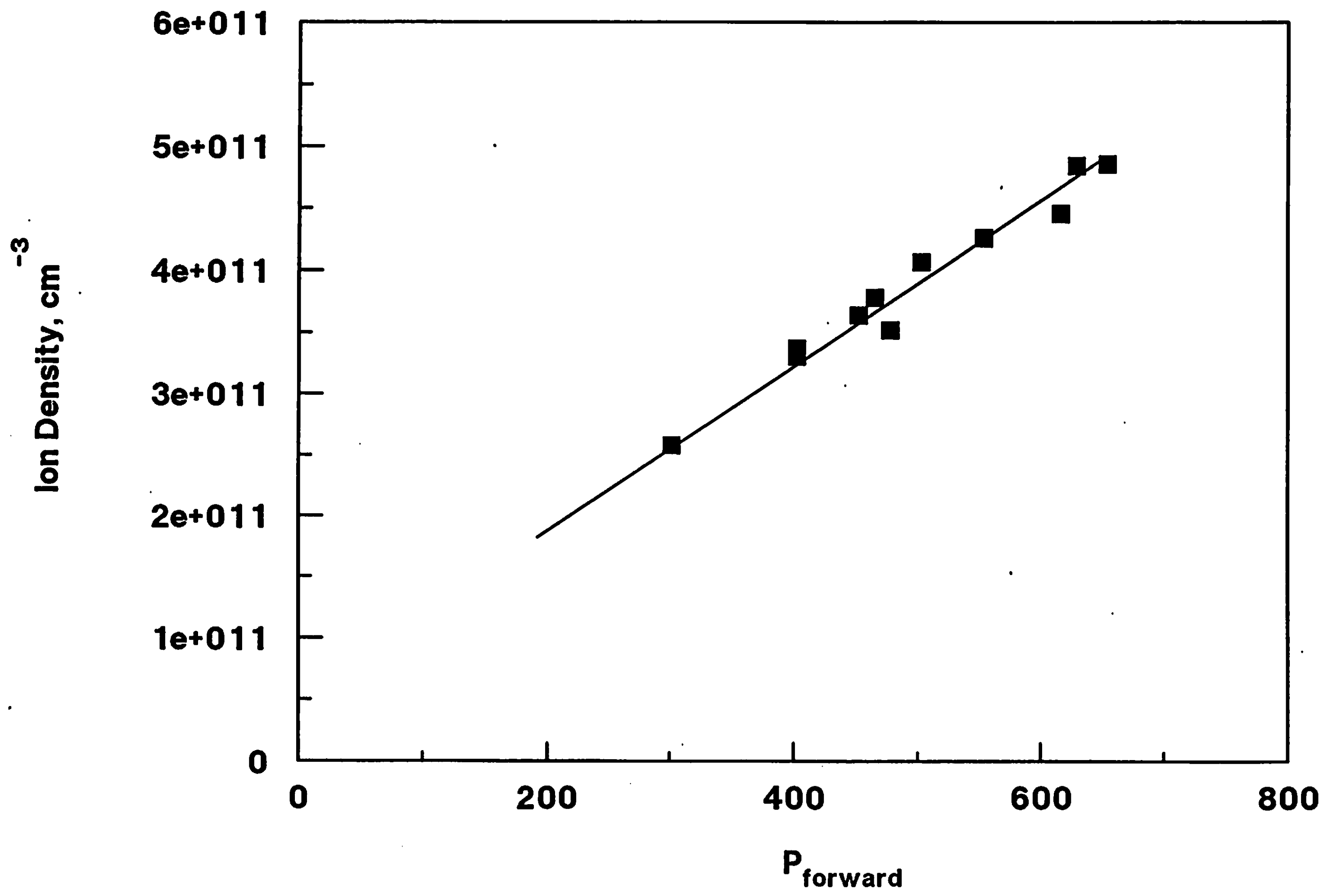

Fig. 2

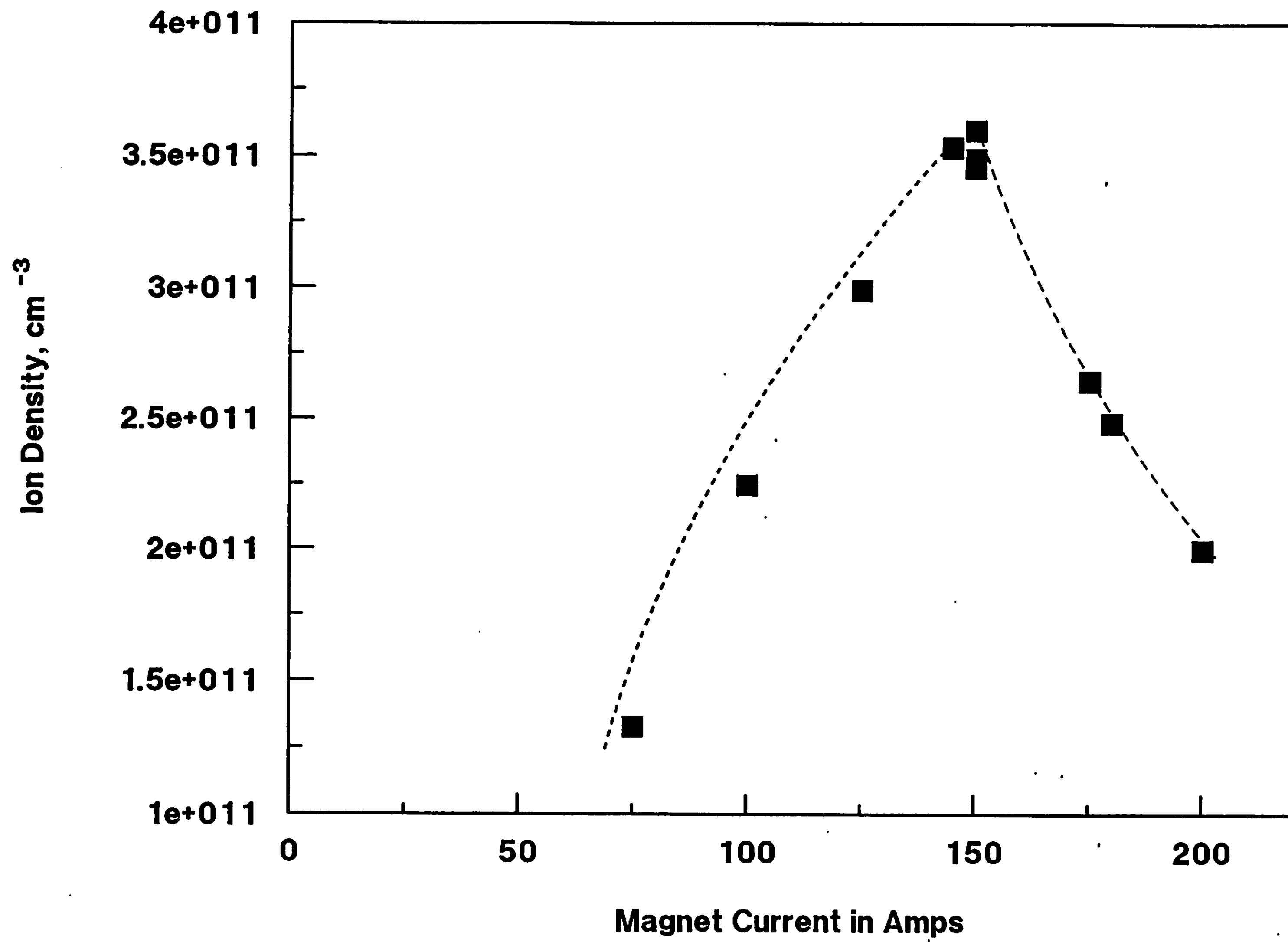

Fig. 3

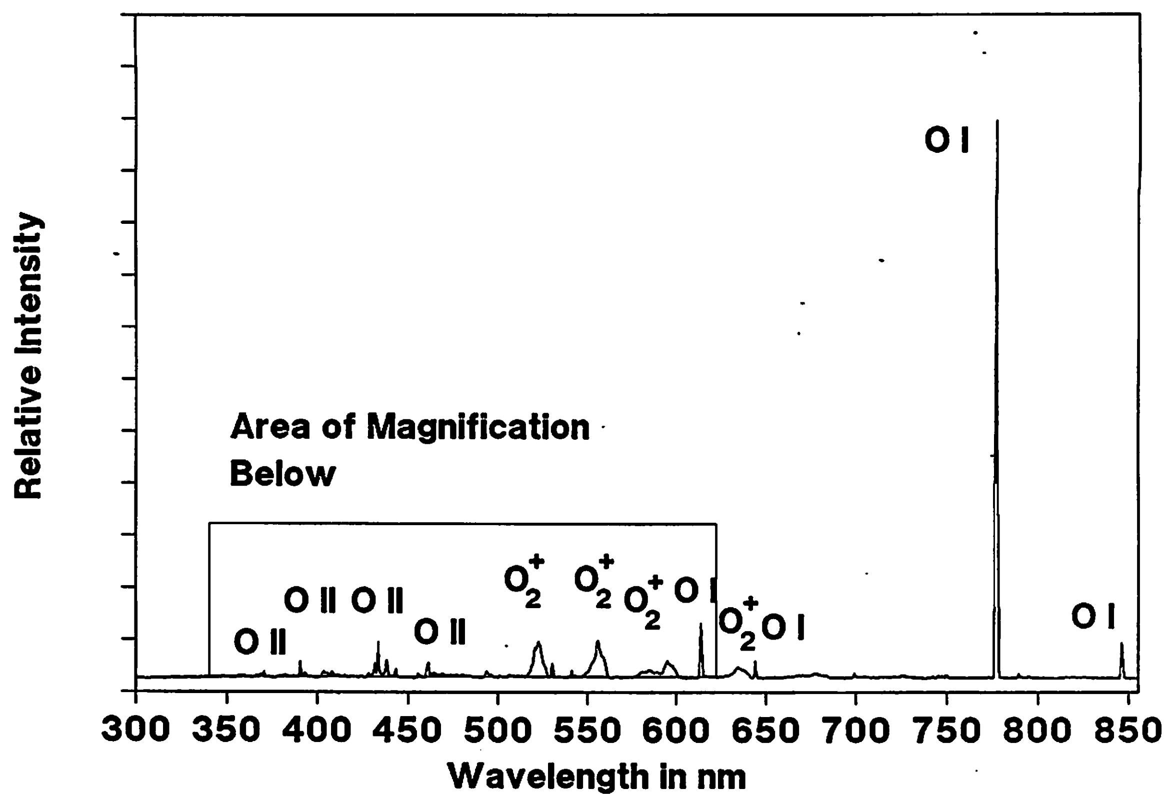

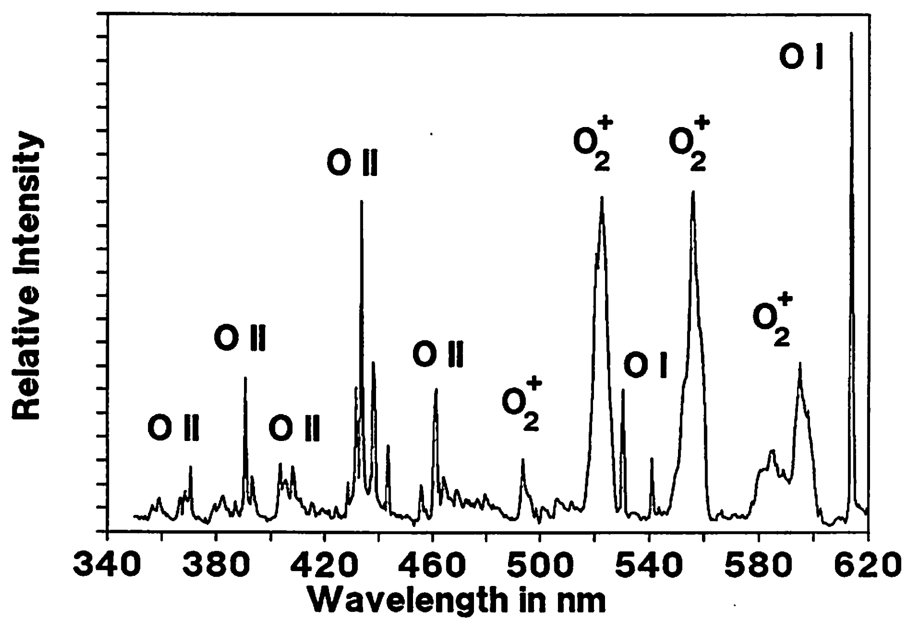

Fig. 4

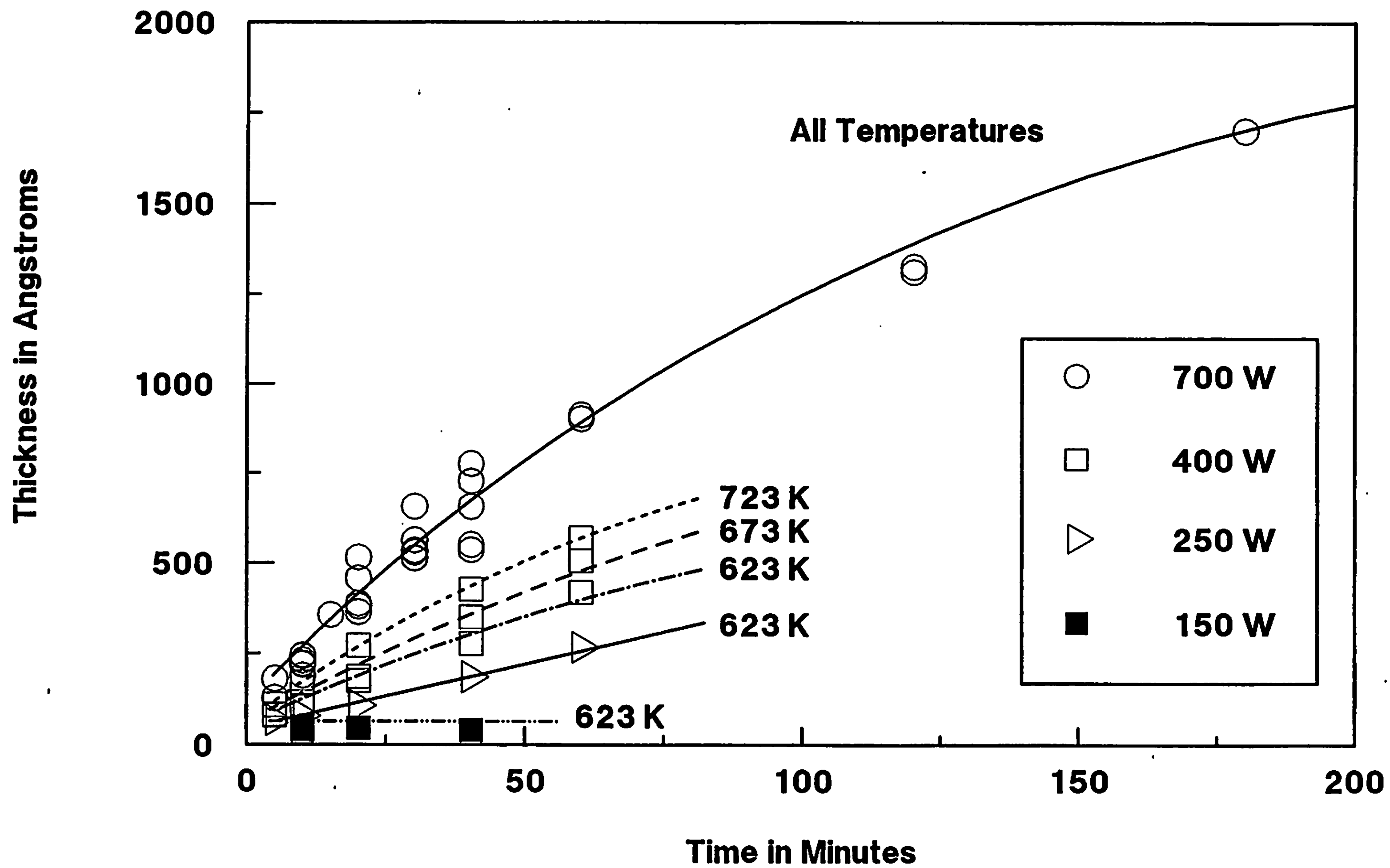

Fig. 5

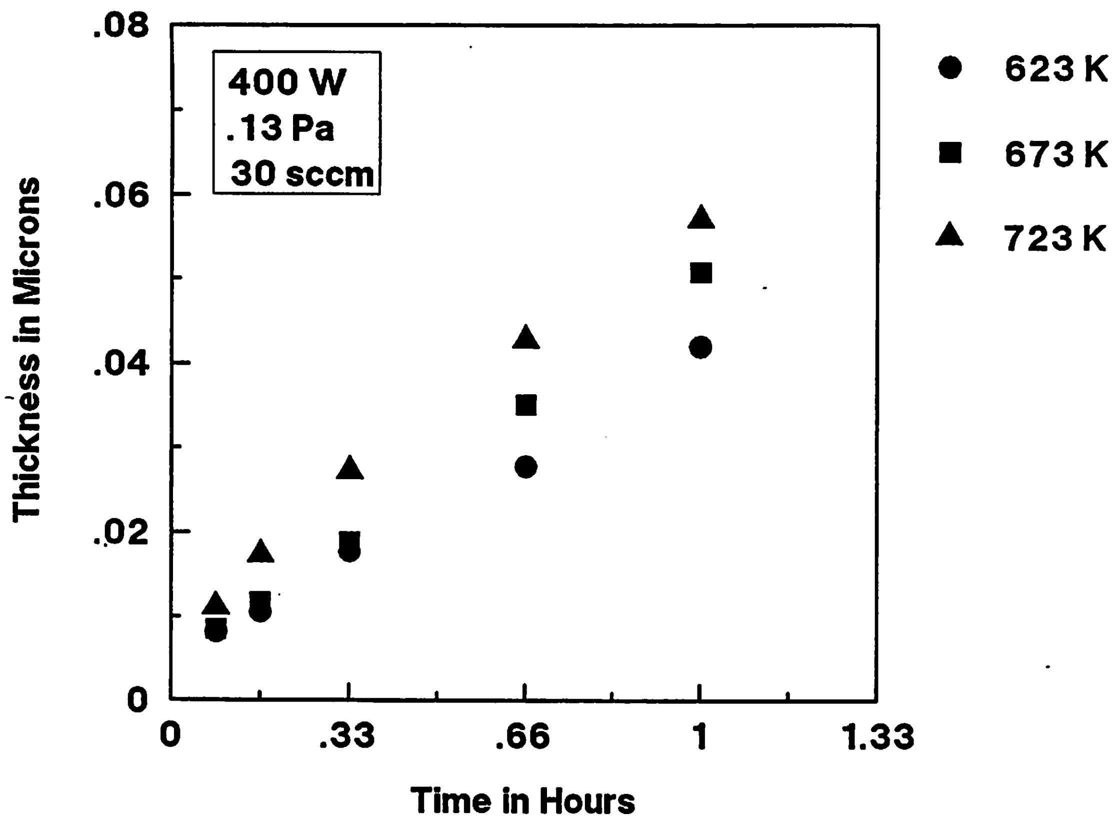

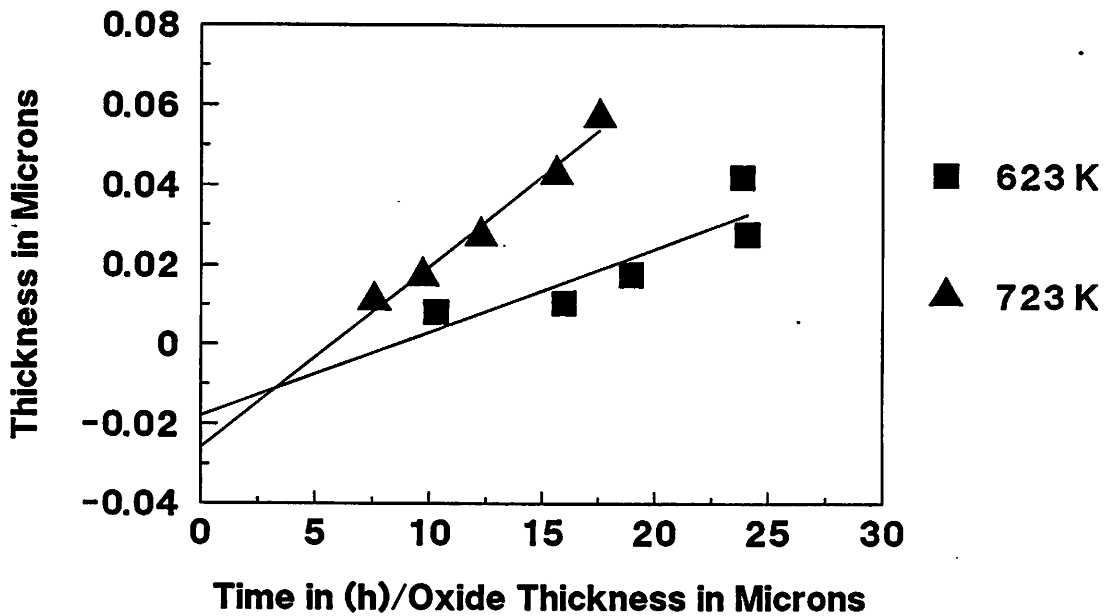

Fig. 6

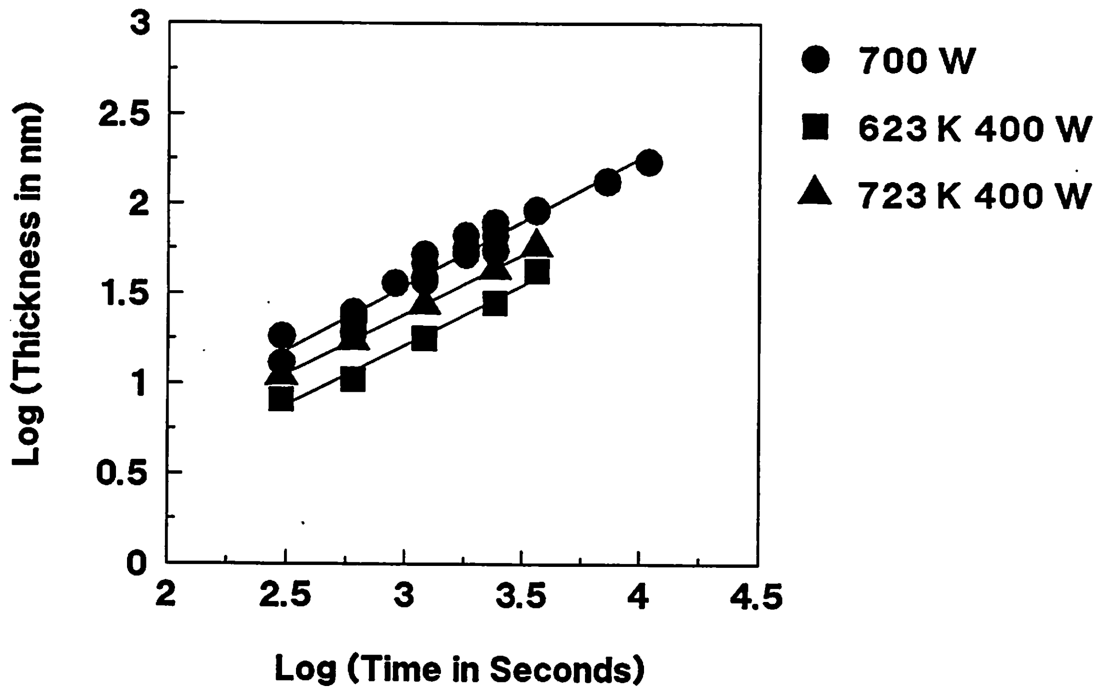

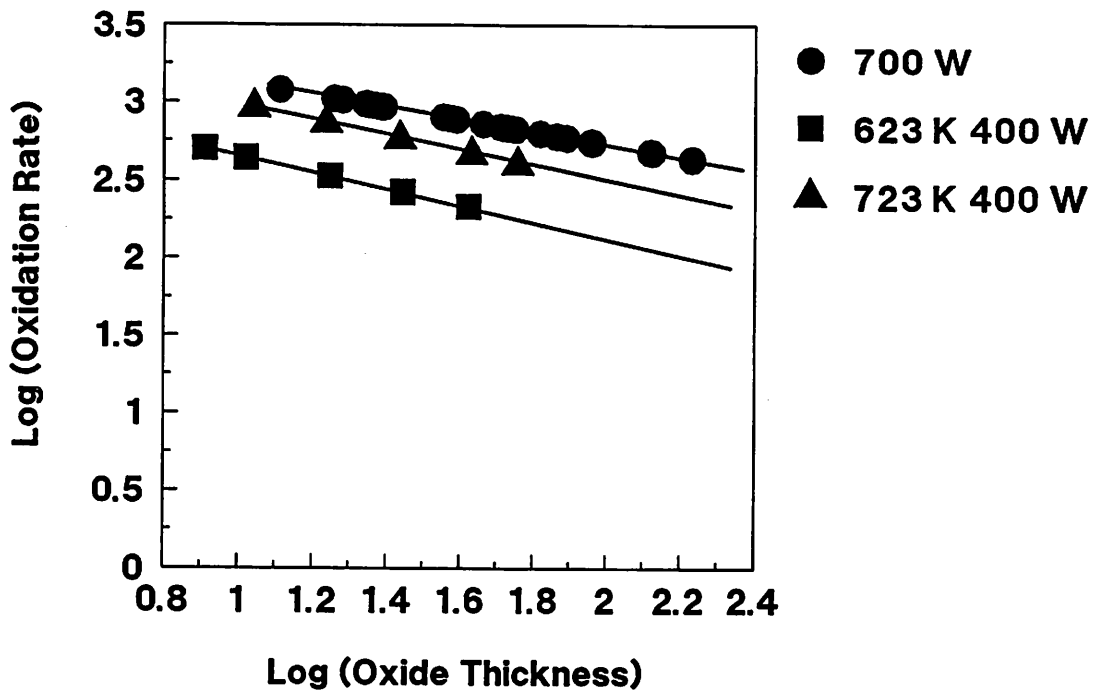

Fig. 7

200
150
100
50
0

Capacitance, pF

298 K
398 K

-6 -4 -2 0 2 4 6

Gate Voltage, V

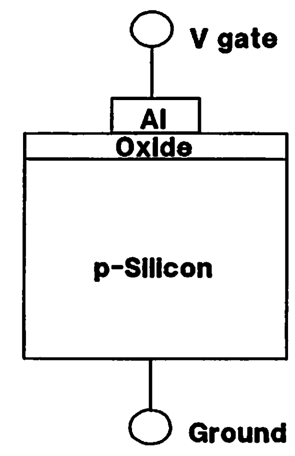

Fig. 8